Empirical energy spectra of neutralized solar wind protons from the lunar regolith

Y. Futaana,[1] S. Barabash,[1] M. Wieser,[1] M. Holmström,[1] C. Lue,[1] P. Wurz,[2] A. Schaufelberger,[2] A. Bhardwaj,[3] M. B. Dhanya,[3] and K. Asamura[4]

Received 28 October 2011; revised 28 March 2012; accepted 28 March 2012; published 16 May 2012.

[1] We present an empirical model of the energy spectra for hydrogen energetic neutral atoms (ENA) backscattered from the lunar surface based on Chandrayaan-1 Energetic Neutral Atom (CENA) observations. The observed energy spectra of the backscattered ENAs are well reproduced by Maxwell-Boltzmann distribution functions. The backscatter fraction is constant and independent of any solar wind parameters and the impinging solar wind angle. The calculated backscatter fraction is 0.19, and the 25% and 75% percentiles are 0.16 and 0.21. The empirical parameters of the Maxwell-Boltzman distribution derived from the CENA imager have no correlations with the upstream solar wind parameters, except for a good correlation between the solar wind velocity and the temperature of the backscattered ENAs. These results suggest that the reflected ENAs have experienced several collisions during the interaction with the loose lunar grains, and are then released into space. The mathematical model of the energy spectra of the backscattered ENAs is expressed by a function of the solar wind flux and velocity, which can be used for future investigations of regolith-solar wind interaction.

Citation: Futaana, Y., S. Barabash, M. Wieser, M. Holmström, C. Lue, P. Wurz, A. Schaufelberger, A. Bhardwaj, M. B. Dhanya, and K. Asamura (2012), Empirical energy spectra of neutralized solar wind protons from the lunar regolith, *J. Geophys. Res.*, *117*, E05005, doi:10.1029/2011JE004019.

1. Introduction

[2] The Moon has neither a global magnetic field [e.g., *Ness et al.*, 1967; *Lin et al.*, 1998] nor a dense atmosphere [e.g., *Stern*, 1999]. Therefore, the solar wind can reach directly to the surface without any disturbances such as a bow shock or a magnetosphere. Localized magnetized regions, called magnetic anomalies, are scattered around the lunar surface [e.g., *Dyal et al.*, 1974; *Mitchell et al.*, 2008]. While they are not very strong compared with the Earth's dipole field, they can, at least on some occasions, produce enough magnetic pressure to balance the solar wind dynamic pressure and may form stand-off mini-magnetospheres [e.g., *Russell and Lichtenstein*, 1975; *Lin et al.*, 1998], and often reflect the solar wind protons above the surface [*Futaana et al.*, 2003; *Lue et al.*, 2011] and thus reduce the backscattered ENA flux from the surface [*Wieser et al.*, 2010].

[3] The Moon is covered by a so-called regolith, which is a layer of loose, heterogeneous material of small size grain [e.g., *Clark et al.*, 2002]. Hydrogen saturation from solar wind protons implantation occurs within 10^4 years at the lunar regolith [*Johnson and Baragiola*, 1991].

[4] *Futaana et al.* [2006] discussed the feasibility of potential experiments of lunar sciences using a modern energetic neutral atom (ENA) instrument. They concluded that ENA instruments can potentially contribute to study the compositional distribution of the regolith using sputtered ENAs, the interaction between the lunar magnetic anomalies and the solar wind, and the solar wind precipitation into the polar regions. *Futaana et al.* [2008] also proposed the potential examination of the exospheric density using the ENAs generated by the charge exchange mechanism between the solar wind protons and the lunar exospheric particles. Considering these ideas, the first ENA instrument in orbit around the Moon, SARA (Sub-keV Atom Reflection Analyzer), was developed and carried into the lunar orbit by the Chandrayaan-1 spacecraft.

[5] Before the arrival of the Chandrayaan-1 spacecraft in lunar orbit, data from plasma sensors on board the Japanese Kaguya spacecraft reported an unexpectedly large proton flux (0.1–1% of the impinging flux) from the lunar regolith [*Saito et al.*, 2008]. This is a big mystery, because the solar wind ions (96% of proton and 4% of alpha particles on average) have been thought to be completely absorbed by the porous regolith surface. SARA on board Chandrayaan-1 [*Wieser et al.*, 2009] and the IBEX-Hi [*McComas et al.*,

[1]Swedish Institute of Space Physics, Kiruna, Sweden.
[2]Physikalisches Institut, University of Bern, Bern, Switzerland.
[3]Space Physics Laboratory, Vikram Sarabhai Space Center, Trivandrum, India.
[4]Institute of Space and Astronautical Science, Japan Aerospace Exploration Agency, Sagamihara, Japan.

Corresponding author: Y. Futaana, Swedish Institute of Space Physics, Box 812, SE-98128 Kiruna, Sweden. (futaana@irf.se)

0148-0227/12/2011JE004019

2009] and IBEX-Lo [*Rodríguez et al.*, 2012] sensors on board the IBEX spacecraft reported a strong flux of ENAs from the lunar surface (∼10–20% of the impinging solar wind flux). A new theoretical model describing the backscattering from regolith has recently been proposed by *Hodges* [2011]. This model produces energy spectra very similar in spectral shape to the observations by SARA, while the absolute flux of backscattered ENAs of solar wind origin predicted from the model is ∼60% for ENAs with energies >25 eV.

[6] It is worth mentioning here that the Martian moon Phobos also backscatters the solar wind protons [*Futaana et al.*, 2010]. Thus, the reflection of the solar wind protons as protons and ENAs are thought to be a general feature of regolith-covered surfaces of the non-magnetized airless bodies.

[7] In this paper, we present a statistical analysis of the energy spectra of the backscattered ENAs from the lunar surface observed by the SARA instrument in order 1) to improve the estimate of the backscatter fraction; 2) to discuss the potential generation mechanism; and 3) to produce an empirical model of the backscattered ENA energy spectrum that can be used in future investigations of solar wind-regolith interactions.

2. Instrument and Data Set

[8] In this paper, we use the data from the Chandrayaan-1 Energetic Neutral Atom (CENA) imager [see *Barabash et al.*, 2009, and references therein]. CENA was a part of the SARA instrument on board the Chandrayaan-1 spacecraft. Chandrayaan-1 was initially inserted into a circular lunar orbit at the height of ∼100 km above the surface, and later the orbit was raised up to the height of ∼200 km. CENA was operational between 28 January and 30 July 2009. CENA measured the ENAs with an intrinsic angular aperture of 10° × 160° divided into 7 angular sectors. At the lunar surface this aperture corresponds to ∼0.6° × 38°, when measured from a spacecraft altitude of 100 km in the case of the nadir pointing. The seven directional channels of CENA provide for an angular resolution of each channel of 6.5° × 45° (FWHM). CENA was capable of mass separation, but in this paper we used only the data obtained in the hydrogen channels.

[9] The maximum extent of the energy range for CENA was 10–3300 eV. During the operations of the CENA sensor, the actual energy steps of the measurement could be selected by command. We used three energy settings during the nominal operations: 11–193 eV (we refer to this setting as energy setting 1 hereafter), 38–652 eV (energy setting 2) and 193–3300 eV (energy setting 3). Each energy setting had 8 logarithmically separated energy bins, covering 15 energy bins by the three energy settings. The energy setting 2 was the default table. The time resolution to obtain one energy spectrum was ∼4 s.

[10] We have to note here briefly about the low energy ENA measurement by the CENA sensor. In the energy range below 25 eV, the measured differential flux has a large uncertainty due to the unavailability of a reliable ionization efficiency of the conversion surface, which is used to ionize incoming ENAs before feeding into an electrostatic analyzer [*Barabash et al.*, 2009]. On the other hand, the conversion surface can ionize an incoming atom with energy lower than its ionization potential (13.6 eV for a hydrogen atom) because ionization by the surface is via electron transfer process, and the energy to ionize the incoming atom is provided by the surface [e.g., *Los and Geerlings*, 1990]. In summary, CENA could in principle measure hydrogen ENAs below 13.6 eV, while the uncertainty of the measurement was large. However, for the current analysis, statistics were derived data from energy setting 2, avoiding the energy range below 25 eV altogether.

[11] The SARA instrument also included a solar wind monitor (SWIM). SWIM was an ion sensor measuring ions in the energy range of 100–3000 eV/q. In this paper, the SWIM data are only used to verify that the Moon was in the solar wind.

[12] In this analysis, we concentrate on the ENA flux measured near the equator because there the ENA flux is the strongest. Near the polar regions, the ENA flux is very close to the detection level of CENA. Thus, we do not use those data. One energy spectrum per one orbit is calculated by the integration of the data obtained within ±30° with respective to the lunar equator. The integration time per orbit was ∼20 min. We use only the central angular channel (CH–3) pointing to the sub-spacecraft location on the lunar surface under the nominal attitude of the spacecraft. We exclude observations conducted under the non-nominal attitude, where the angle between the center viewing vector and the nadir direction is more than 10° off. The use of the central channel gives us only information about the ENAs flying toward the zenith direction. Note that the impinging solar wind beam direction with respect to the surface normal changes from orbit to orbit according to the solar zenith angle of the backscattering point.

[13] In the later analysis, we also use the level-2 (L2) data of the ACE spacecraft to compare the upstream solar wind plasma and magnetic field parameters to the backscattered ENAs. The plasma parameters measured by ACE are shifted in time by considering the velocity of the solar wind (V_{sw}) and the distance between the ACE and the Moon (L) at the time of the observation. The typical time shift, $\langle t \rangle = (L/V_{sw})$, is 1–1.5 h. The time shift creates an uncertainty in the upstream condition at the Moon, in particular for single event studies. However, the uncertainty becomes smaller as the number of orbits increases [*Collier et al.*, 1998; *Paularena et al.*, 1998].

3. Observed ENA Spectrum and Fitting

[14] Figure 1 shows the differential flux of ENAs observed by CENA. In this case, the full energy spectra (15 energy steps) can be reconstructed from three consecutive orbits (orbits 2998–3000). For orbit 2998 (between 23:44:43UT on 17 July 2009 and 00:05:43UT on 18 July 2009), CENA used the energy setting 1 measuring the lower energy part of the ENA spectrum. For orbit 2999 (between 01:52:30 and 02:10:58UT on 18 July 2009), the energy setting 3 was used to measure the high energy part. Then, for orbit 3000 (04:00:18–04:21:18 on 18 July 2009), the energy setting 2 was used for the intermediate energy range. The energy ranges for different energy settings are drawn in Figure 1. During this period, no strong solar wind changes have been found according to the time-shifted WIND data (the solar

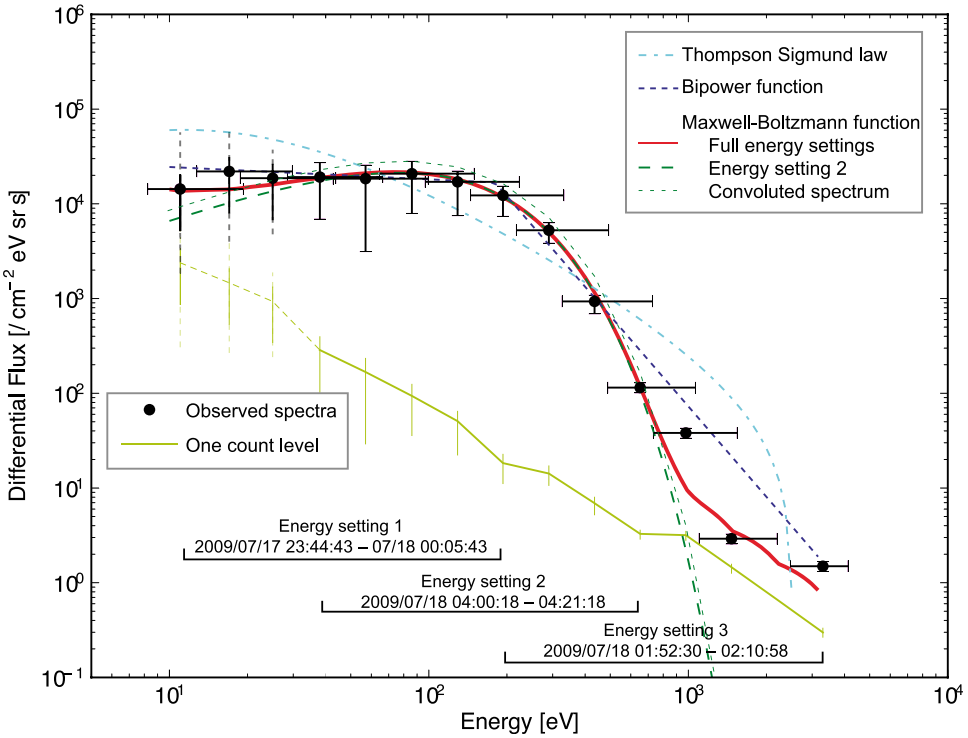

Figure 1. Differential flux of the observed backscattered ENAs (black circles). Data for three consecutive orbits (2998–3000) are averaged. Error bars correspond to the energy resolution (x-axis) and the error in flux (y-axis) mainly due to the uncertainty of the ionization efficiency of the conversion surface of the CENA sensor. Particularly, no reliable ionization efficiency is available for low energy channels <25 eV, and thus, the error bars may be underestimated in the low energy channels <25 eV (dashed lines). The energy ranges corresponding to the energy settings 1–3 of the CENA sensor are also indicated. The yellow line indicates the one count level based on the accumulation time, the energy resolution and the ionization efficiency. There may be large systematic uncertainties below 25 eV. Three different types of the fitting were examined (see text for details): the Thompson-Sigmund law (light blue line), the bi-power law (blue line), and the Maxwell-Boltzmann distribution (red line). In addition, a Maxwell-Boltzmann distribution fitted only to the energy setting 2 data (38–652 eV) is shown by the green dashed line. A Maxwell-Boltzmann distribution convolved with relatively wide energy resolution and response functions [*Kazama*, 2006] is also shown by the green dotted line.

wind density was 4.8–6.0 cm^{-3}, the velocity 290–320 km/s and the temperature 4.7–6.0 eV; note that for this time period the density and temperature data from ACE is missing, and we therefore refer to WIND data here); this allowed us to average the spectra from three consecutive orbits into one energy spectrum.

[15] To model the energy spectrum of the backscattered ENAs from the lunar surface, we first examined three possible mathematical functions. The parameters of each function are then optimized to reproduce the observed energy spectrum.

[16] The first model spectrum follows the Thompson-Sigmund law [*Thompson*, 1968; *Betz and Wien*, 1994; *Wurz and Lammer*, 2003; *Futaana et al.*, 2006]. This function is widely used for approximating sputtered atoms from solid surfaces. The energy distribution can be written as

$$F_{\mathrm{ts}}(E) = nC\frac{E}{(E+E_b)^3}\left(1-\sqrt{\frac{E+E_b}{E_i'}}\right) \quad (1)$$

where E_b is the binding energy of an atom at the surface (the sublimation energy, typically several electron volts), n is the number density of sputtered atoms, and C is the normalization constant for the distribution [*Wurz et al.*, 2007]. E_i' is equal to the maximum energy that a sputtered atom can have:

$$E_i' = 4E_i\frac{M_1M_2}{(M_1+M_2)^2} \quad (2)$$

where E_i is the energy of the incident atom or ion, and M_1 and M_2 are the masses of the incident and surface atoms, respectively [*Betz and Wien*, 1994]. The corresponding differential flux can be written as

$$J_{\mathrm{ts}}(E) = \sqrt{\frac{2E}{m}}F_{\mathrm{ts}}(E) \quad (3)$$

Here the parameters E_b, E_i' and nC are to be optimized to fit the observed energy spectrum.

[17] The second model spectrum used follows a bi-power law. There are no specific physical reasons to use this spectrum. However, such a spectral shape has been used earlier for scientific discussion of the ENA energy spectra emitted from planetary atmospheres [e.g., *Galli et al.*, 2008].

$$J_{\mathrm{bp}}(E) = \begin{cases} k_0 E^{-r_0} & (E \le E_0) \\ k_1 E^{-r1} & (E > E_0) \end{cases} \tag{4}$$

where E_0 is the roll-over energy calculated from other parameters as

$$\ln(E_0) = -\frac{\ln(k_0) - \ln(k_1)}{r_0 - r_1} \tag{5}$$

Thus, there are four parameters (k_0, k_1, r_0 and r_1) to be optimized to fit the observed spectra.

[18] The last model spectrum to examine is the Maxwell-Boltzmann distribution. This spectrum may be realized if the ENAs are randomly distributed by multiple collisions at the surface. The velocity distribution of the Maxwell-Boltzmann distribution function is

$$f_{\mathrm{mx}}(v) = n_0 \left(\frac{m}{2\pi kT}\right)^{\frac{3}{2}} \exp\left(-\frac{mv^2}{2kT}\right) \tag{6}$$

and the corresponding differential flux is thus described as

$$J_{\mathrm{mx}}(E) = \frac{2n_0}{m^2} \left(\frac{m}{2\pi kT}\right)^{\frac{3}{2}} E \exp\left(-\frac{E}{kT}\right) \tag{7}$$

where T is the absolute temperature and n_0 is the number density.

[19] To optimize the parameters for each spectrum, we used the least square method. The optimization was conducted in the count rate domain because the count rate is the observed quantity. This means that we first calculated the expected count rate, $C_{\mathrm{exp}}(E_i; \mathbf{p})$, where E_i is the energy step for the i-th energy bin and $\mathbf{p}$ denotes the set of parameters, from the parametric differential flux function using CENA's geometric factor and its efficiency. By using least squares method, we then searched for the best fit parameters, $\mathbf{p}_{\mathrm{best}}$, to minimize the difference between the expected count rate and the observed count rate,

$$\varepsilon(\mathbf{p}) = \sum_i \left(C_{\mathrm{exp}}(E_i, \mathbf{p}) - C_{\mathrm{obs}}(E_i)\right)^2 \tag{8}$$

where $C_{\mathrm{obs}}(E_i)$ is the observed count rate at the i-th energy channel. We added a constant background as an additional free parameter for fitting.

[20] The fitting results are superimposed in Figure 1. The light blue line is for the Thompson-Sigmund law with the best fit parameters E_b = 11.8 eV and E_i' = 2.54 keV. Both parameters are too far from realistic values for atoms sputtered by the solar wind from a solid surface and the observed energy spectrum cannot be reproduced by the Thompson-Sigmund spectrum very well. The fitted spectrum with the bi-power law is shown by the blue line in Figure 1 with the best parameters for k_0 and k_1 being 3.3×10^4 and 2.41×10^{11} [/cm^2 sr eV s] and r_0 and r_1 equal to -0.13 and -3.2, respectively. The bi-power low reproduces the observed energy spectra better than the Thompson-Sigmund law. However, the red line, which shows the Maxwell-Boltzmann distribution with the parameters of n_0 = 4.01 cm^{-3} and kT = 76.9 eV, provides the best fit among the three functions. We checked all the occasions where we can obtain a full energy spectrum (15 energy steps between 11 and 3300 eV) from three consecutive orbits. In all these cases, the Maxwell-Boltzmann distribution provides the best fit of the observed ENA energy spectrum, even the Maxwell-Boltzmann distribution needs the smallest number of free parameters among the three examined distributions.

[21] However, the opportunities when we can reconstruct a full spectrum using 15 energy steps are limited. The energy setting 2 was the default setting for nominal CENA operations, and therefore, the largest fraction of the data was obtained using the energy setting 2. For statistical analysis, using the energy setting 2 data provides an advantage. The tradeoff using the data from energy setting 2 is that the setting only provides 8 energy steps between 38 and 652 eV. Therefore, we examine here whether the energy setting 2 data can be used to parameterize the full energy spectrum. The green curve in Figure 1 shows the best fit using only the 8 energy steps in energy setting 2 out of the full 15 energy steps. There are small discrepancies in the lower and higher energies, but these may come mainly from contributions from the background. The main peak of the energy spectrum can be reproduced reasonably well from energy setting 2 data. The parameter differences are indeed quite small. Those derived from the energy setting 2 are n_0 = 4.08 cm^{-3} and kT = 76.9 eV. We also verified that for the other opportunities we could obtain full energy spectra, and the average error between the energy setting 2 and full energy steps is $\sim$1.4% for the parameter n_0 and $\sim$0.56% for kT. Thus, we can conclude that the fits for the full energy spectrum can be accurately inferred from the data obtained only by the energy setting 2, and we will use such data for the following statistical analysis.

[22] Using the above method, we conduct the parameter calculation for all the available orbits. We only use the data obtained when the Moon was in the solar wind (not in the magnetosheath nor in the magnetosphere) determined from SWIM data. The data obtained from foreshock region are included in the following analysis. Suspicious orbits, i.e., when we cannot clearly tell whether the Moon was in the magnetosheath or the solar wind, are excluded. We also exclude data that were contaminated by strong background. We also remove the data that contain a very low count rate, i.e., we only used the data when the counts in all the energy bins in the energy setting 2 were at least 1. Moreover, as described in the data set section, we only used periods when the spacecraft was in the nadir pointing mode (i.e., the FoV used for this analysis is pointing toward the surface), and the observations were within $\pm 30^\circ$ with relative to the lunar equator. After these exclusions from the full mission data set, a successful fitting could be carried out using 108 orbits.

[23] The mathematical formulation of the velocity distribution functions, energy distribution functions and the

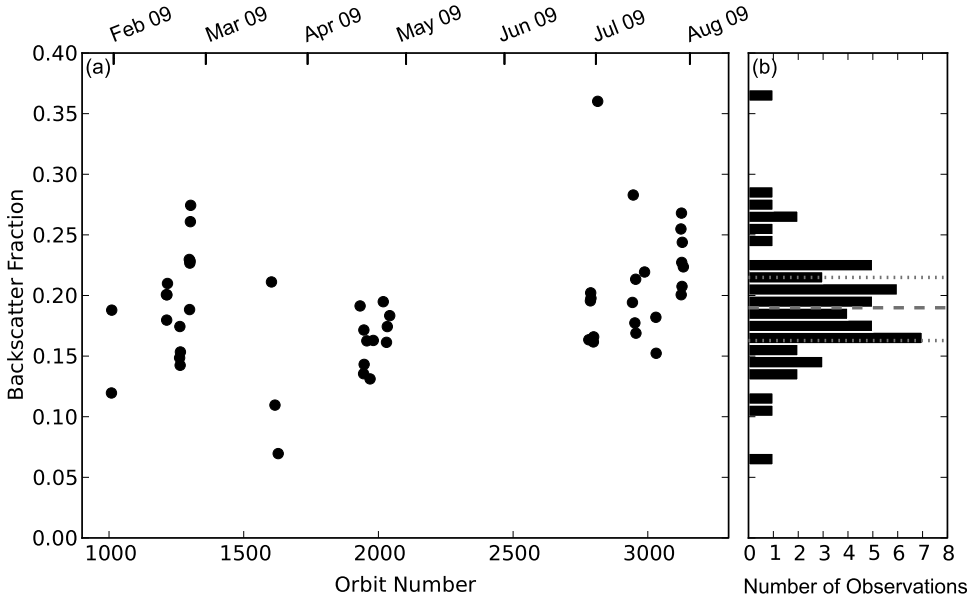

Figure 2. (a) Time series of the backscatter fraction. A backscatter fraction is calculated by the integration over ~20 min each orbit near the lunar equator. (b) The histogram of the backscatter fraction. Median (dashed line) is 0.19 and the 25% and 75% percentiles (dotted lines) are 0.16–0.21.

differential energy flux for Maxwell-Boltzmann distributions can be respectively written as follows:

$$f_{\mathrm{mx}}(v) = n_0\left(\frac{m}{2\pi kT}\right)^{\frac{3}{2}}\exp\left(-\frac{mv^2}{2kT}\right) \tag{9}$$

$$F_{\mathrm{mx}}(E) = n_0\sqrt{\frac{2E}{m}}\left(\frac{m}{2\pi kT}\right)^{\frac{3}{2}}\exp\left(-\frac{E}{kT}\right) \tag{10}$$

$$J_{\mathrm{mx}}(E) = \frac{2n_0}{m^2}\left(\frac{m}{2\pi kT}\right)^{\frac{3}{2}}E\exp\left(-\frac{E}{kT}\right) \tag{11}$$

[24] By taking the median of the best parameters of 108 data sets, we obtain n_0 = 2.98 cm^{-3} and kT = 93.0 eV. The 25% and 75% percentile ranges are n_0 = 2.06–5.53 cm^{-3} and kT = 81.7–111 eV. Note that the ENA distribution functions are conserved between the observation position and the lunar surface because of the collisionless trajectories for ENAs from the lunar surface to the spacecraft. Thus, the expressions can also be applied for ENAs at the surface just after the backscattering. Moreover, the ENAs are not in the thermal equilibrium with each other because of the lack of gas-phase collisions, and therefore, one must not consider the parameter T as a temperature in a usual sense such as the case of a thermal gas, but kT is a measure of the width of the energy distribution. The parameter n_0 does not directly correspond to the ENA density because the angular response should be taken into account, while in this study we only consider the ENAs flying normal to the lunar surface. If we assume isotropic angular distribution, the backscattered ENA density, n_{ENA}, is calculated to be $n_0/2$, because only the upstreaming ENAs will be integrated.

[25] In the following we consider the energy resolution of the CENA sensor and its response functions. Precisely speaking, to derive the energy spectrum from the observed counts, we have to deconvolve the energy response because the CENA sensor has a relatively wide and asymmetric energy response [*Kazama*, 2006]. However, in this analysis we used the simplest approach, i.e., we assumed that the energy resolution is small enough that the count observed is from the central energy of the sensor settings. Thus, we examine, using response functions by *Kazama* [2006], the effect of the relatively wide energy spectra. The green dotted curve in Figure 1 shows the fit of the energy spectra shape of (11) convolved with the CENA energy response. Qualitatively, the shape of observed energy spectrum using the simplest approach agrees well with the convolved model spectrum: qualitatively, the total flux is slightly underestimated without considering the energy resolution (~25% relatively), while the temperatures do not differ by much.

[26] The fitted parameters are expected to primarily depend on the solar wind conditions. In the following section, we will discuss the dependencies, and try to improve the empirical spectrum.

4. Backscattering Fraction

[27] By integrating the empirical energy spectra, we can derive the statistical value for the backscatter fraction. Figure 2a shows the backscatter fraction as a function of the observation time (orbit number of the spacecraft). Here, the backscatter fraction, r, was calculated using the following formula:

$$r = \int f_a(\Omega)\mathrm{d}^2\Omega\frac{\int_0^\infty J_{\mathrm{mx}}(E; n_{\mathrm{best}}, T_{\mathrm{best}})\mathrm{d}E}{F_{\mathrm{sw}}\cos(\mathrm{SZA})} \tag{12}$$

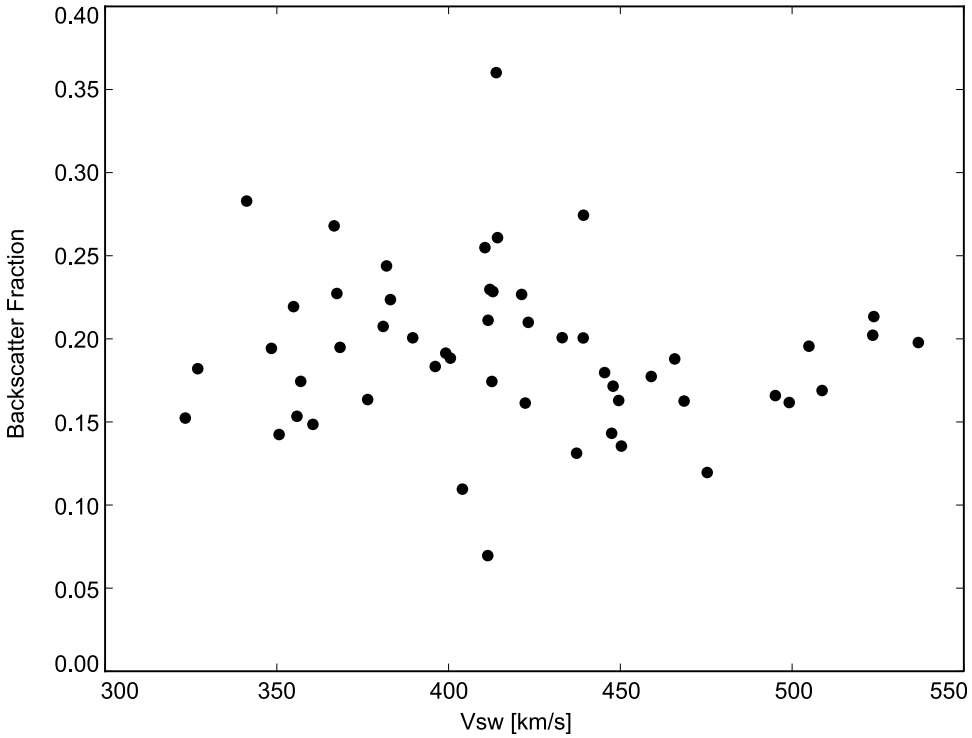

Figure 3. The dependence of the backscatter fraction of the ENAs to the solar wind velocity.

where f_a is the angular distribution function of ENAs scattered from the lunar surface, n_{best} and T_{best} are the derived best fit parameters, F_{sw} is the solar wind proton flux observed by ACE and shifted in time to the arrival at the location of the Moon, and SZA is the solar zenith angle of the reflection point, which is taken as the intersection between the FoV center of the sensor and the lunar surface. For simplicity, we assume an isotropic angular distribution function as was used in *Wieser et al.* [2009], which leads to $f_a = 1$. Thus, the integral of the angular distribution in (12) evaluates to 2π for the integration over the zenith hemisphere. The complete angular distribution is given in *Schaufelberger et al.* [2011].

[28] Due to the limitation of the CENA operation, data of the orbits between 2100 and 2700 are missing. After orbit 2496, the spacecraft was raised up to 200 km altitude. In addition, because sometimes the corresponding ACE L2 data for the solar wind ions are missing, we can calculate the backscatter fraction only for 52 orbits. While there are a few outlying values, the backscatter fraction is fairly constant over the period of observations. The median of backscatter fraction is 0.19 and the range of 25% and 75% percentile is 0.16–0.21 (see Figure 2b). Considering the 95% confidence as in *Wieser et al.* [2009], the median backscatter fraction would range 0.03–0.34. The backscatter fractions could be underestimated because of relatively wide energy response of CENA instrument. Accounting for the energy response of the CENA sensor, the average backscatter fraction raises up to ~0.24.

[29] These values are in good agreement to the first report of the backscatter fraction from a case study by *Wieser et al.* [2009]. They integrated over the energy spectra above 25 eV for the energy setting 2, and concluded that up to 20% of protons are backscattered as ENAs. Here we integrated over the full energy range. However, if we limit the lower energy to 25 eV for the integration, these values do not decrease significantly. Note that *Wieser et al.* [2009] discussed the backscatter fraction using the data downstream of the Earth's bow shock, i.e., when the Moon was in the magnetosheath, and therefore these data are not included in the statistical analysis of this paper.

[30] To investigate what controls the backscatter fraction, we compared it with the solar wind plasma parameters, such as density, velocity, temperature, the interplanetary magnetic field and the fraction of alpha particles. We could not find any correlations between the backscatter fraction and the solar wind conditions. Figure 3 shows, as an example, the dependences of the backscatter fraction on the solar wind velocity. In Figure 4, the backscatter fraction is compared with the solar zenith angle, which is directly considered to represent the impinging angle to the lunar surface normal. A slight decrease for higher solar zenith angles could possibly be identified, but this is not significant.

[31] We did not find any correlations between the backscatter fraction derived from the Maxwell-Boltzmann fitting and any of the solar wind parameters. The lack of correlations indicates that the reflection process at the regolith surface is not strongly controlled by the upstream solar wind conditions. Due to the low statistics of this small data set, we cannot look for a correlation with local geodetic features and local regolith features, for example, the local topography, the porosity, the grain size distribution, the magnetization, and the composition in this analysis. This will be future studies.

[32] Recently, *Hodges* [2011] reported a new theoretical model of the backscattered ENAs from the lunar regolith. They used a Monte Carlo approach tracing the solar wind protons that experience charge exchange neutralization, an

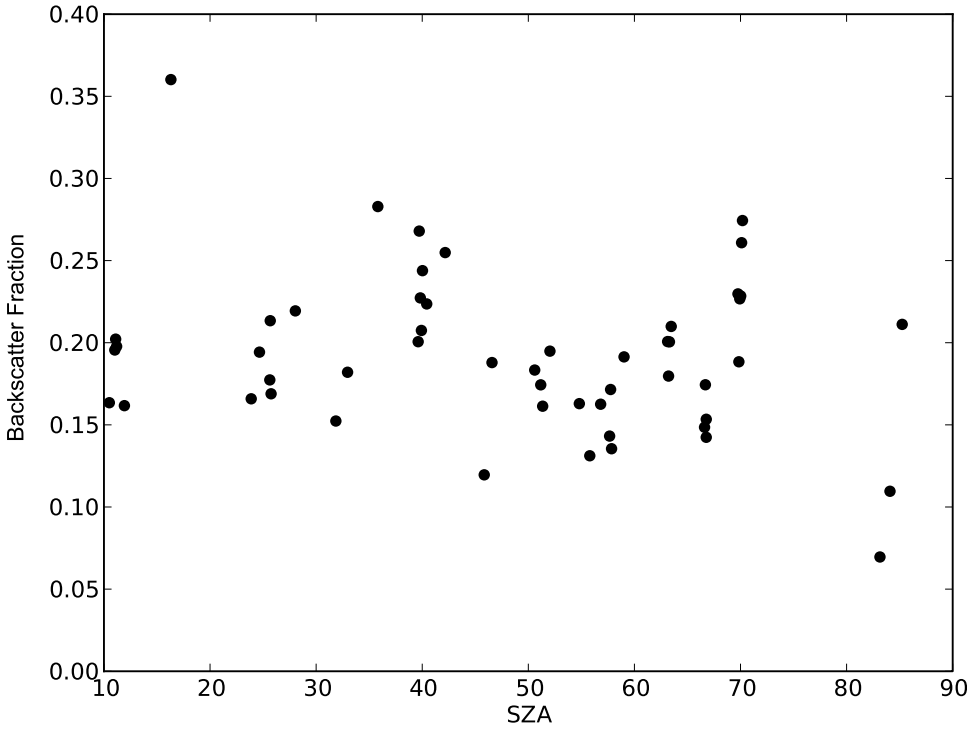

Figure 4. Solar zenith angle dependence of the backscatter fraction.

inter-atom transport for fast H in the subsurface layers of soil grains and rocks, and multiple encounters of free H with loosely packed soil grains. The resulting energy spectra obtained by *Hodges* [2011] resemble the spectral features of the observed one by *Wieser et al.* [2009], particularly for the high energy part (>100 eV). However, the main discrepancy was the backscatter fraction, where *Hodges* [2011] obtained a backscatter fraction of ∼0.60 for energies exceeding 25 eV, which was much higher than the observed value of ∼0.20 (0.03–0.35 with 95% confidence) reported by *Wieser et al.* [2009]. *Hodges* [2011] mainly attributed the discrepancy to the overestimation of the impinging shocked solar wind proton flux measured by the SWIM sensor. However, in the present study we used ACE solar wind data and the observed backscatter fraction in the undisturbed solar wind is still on average ∼0.19 (0.03–0.34 with 95% confidence), or ∼0.24 if we account for the relatively course energy resolution of the CENA sensor. Nevertheless, it is more important to state here that the backscatter fraction does not depend on the solar wind parameters.

5. Empirical Energy Spectrum of Lunar ENAs

[33] One of the final goals of this paper is to express the empirical spectra as a function of the upstream solar wind parameters. Equations (9)–(11) have two free parameters. The rather constant backscatter fraction derived in the previous section can be used as one parameter in combination with the solar wind flux. The second parameter is the temperature, T, inside the exponential term of equations (9)–(11).

[34] Thus, we also checked the backscattered ENA temperature dependence on the upstream solar wind condition. We found a strong correlation between the temperature of the backscattered ENAs and the solar wind velocity (Figure 5). From Figure 5, the temperature is proportional to the solar wind velocity as

$$kT[\text{in eV}] = V_{\text{SW}}[\text{in km/s}] \times 0.273 - 1.99 \tag{13}$$

or in the MKSA unit system, (13) can be written as

$$T[\text{in K}] = V_{\text{SW}}[\text{in m/s}] \times 3.17 - 2.31 \times 10^4 \tag{14}$$

and the correlation coefficient is $R = 0.94$. There is also a weaker correlation ($R = 0.6$) between the solar wind thermal velocity and the backscattered ENA temperature. Because of the lower coefficient and the well-known correlation between solar wind temperature and the solar wind velocity [e.g., *Lopez and Freeman*, 1986], the primary contribution to the backscattered ENAs is expected to be the solar wind velocity. No significant correlation with any other solar wind parameter, such as density or interplanetary magnetic field strength, is found.

[35] Considering two results that 1) the backscatter fraction is constant independent of the solar wind parameters and 2) the backscattered ENA temperature is proportional to the solar wind velocity, we can use the flux of the solar wind at the lunar surface, $F_{sw} = n_{sw} \times V_{sw} \times \cos(\text{SZA})$, and the velocity of the solar wind, V_{sw}, as the primary parameters to make empirical models. The empirical forms of the velocity distribution function, and the differential flux in the MKSA system, by

$$f(v) = \frac{rF_{\text{SW}}}{4\pi}\left(\frac{m}{kT}\right)^2 \exp\left(-\frac{mv^2}{2kT}\right) \tag{15}$$

$$J(E) = \frac{rF_{\text{SW}}}{2\pi}\frac{E}{(kT)^2}\exp\left(-\frac{E}{kT}\right) \tag{16}$$

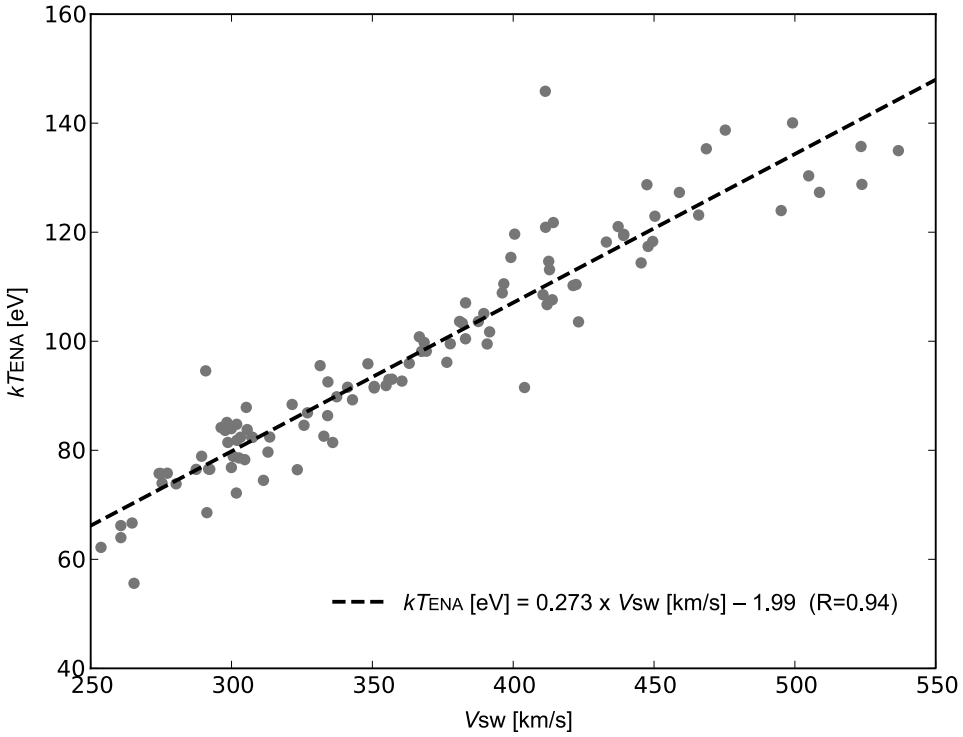

Figure 5. Correlation between the absolute temperature derived by fitting the observed data and the upstream solar wind velocity measured by ACE. The linear regression line is also plotted as a dashed line.

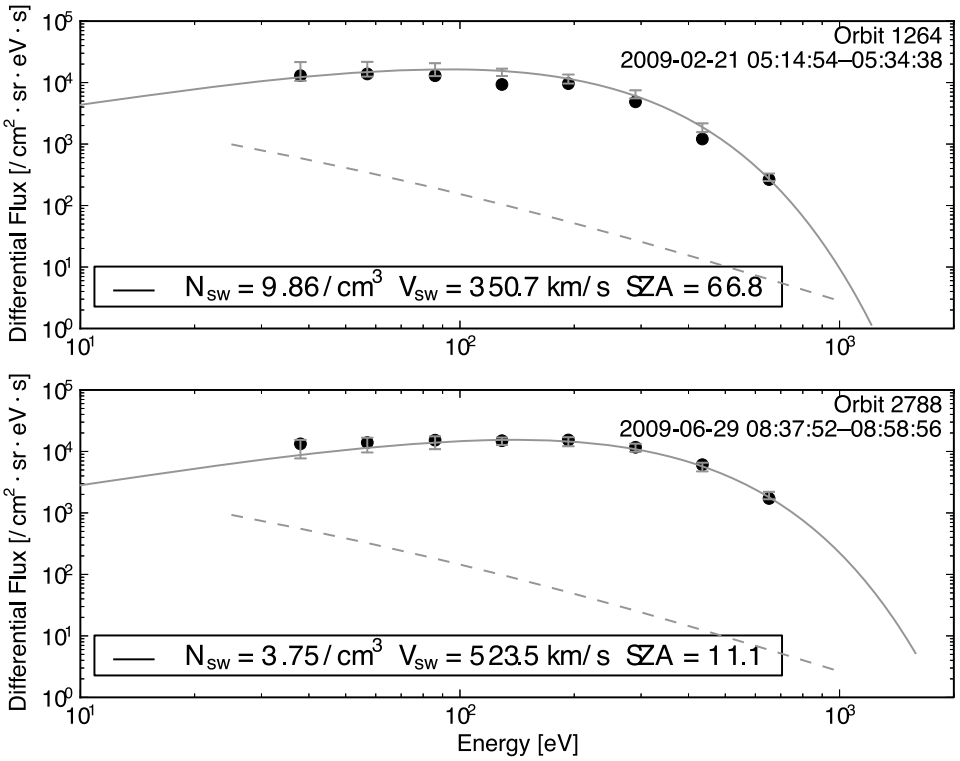

Figure 6. The observed energy spectra (filled circles) for two orbits and the energy spectra calculated the empirical model of the backscattered ENAs (solid line). Dashed lines are the instrument one count levels. Orbits 1264 (05:14:54–05:34:38 on 21 February 2009) and 2788 (08:37:52–08:58:56 on 29 June 2009) are shown. The inputs for the empirical model are the time-shifted ACE data and the solar zenith angle to calculate the solar wind fluxes at the surface. The error bar on the calculated empirical model is derived from the relative error between the fluxes from empirical model and observation for 52 examined cases.

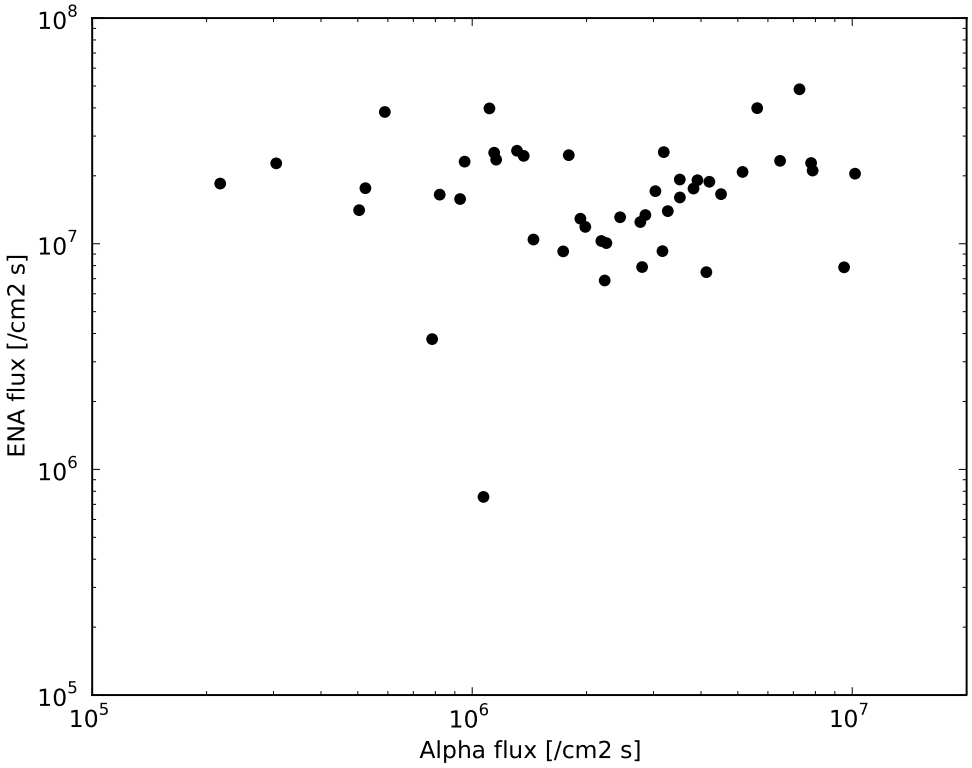

Figure 7. The total ENA flux as a function of the solar wind alpha particle flux. The solar wind alpha particle flux was deduced from the ratio of alpha particles to protons in the ACE L2 data.

where T is expressed in Kelvin from equation (14) and V_{sw} in m/s, and r is the backscatter fraction of 0.19.

[36] The comparison between the observed differential flux and the one calculated from the upstream conditions is shown in Figure 6. We first chose two orbits (1264 and 2788), and reproduced the energy spectra using equation (16) with the upstream solar wind parameters from time-shifted ACE data to compare them with the observed data.

[37] The observation data and the empirical models agree quite well. When we plot the energy spectrum derived from the empirical model, no background of sensor origin is added. Thus, there are small underestimations particularly in the lowest energy channels (25 eV) due to the background.

6. ENA Generation Mechanism

[38] We can rule out that the origin of these ENAs lies in ion induced sputtering from the surface because the expected energy distribution differs significantly from the observed one [cf. *Wurz et al.*, 2007]. Moreover, the composition of the observed ENAs disproves the sputtering origin. A regolith grain saturated with solar wind protons contains about 10^{19} hydrogen atoms per cm^3 compared with the total number density of the order of 10^{23} atoms per cm^3 of regolith, of which about half is oxygen [*Wurz et al.*, 2007]. This means that the hydrogen fraction in the observed ENAs must be quite small (0.01%) in the observed ENAs if they are produced approximately in stoichiometric quantities by sputtering. In addition, the lack of the correlation between the observed ENA flux to the solar wind alpha particle flux shown in Figure 7 disproves the sputtering origin. Here the solar wind alpha particle flux was calculated from the fraction of alpha particles and the proton density in the ACE L2 data and the velocity of the alpha particles is assumed to be the same as that of the protons. While alpha particles are expected to contribute 30% of the solar wind sputter yield [*Wurz et al.*, 2007], we do not see an obvious correlation between the reflected ENAs and the alpha particle flux.

[39] A possibility for the ENA generation by sputtering of the regolith particles after multiple collision cascades (sometimes called spike regime [e.g., *Betz and Wien*, 1994]) can also be ruled out. Even though the mechanism may explain the observed Maxwell-Boltzmann spectrum shape of the ENAs due to the local thermal equivalent assumption in the spike regime, the temperature measured in this study is too high ($\sim$100 eV = $\sim 10^6$ K) to realize the local thermal equivalent at the lunar regolith. Moreover, the collision cascade is thought to happen only for impinging particles with energies higher than 100 keV, which cannot be applied to the solar wind interaction with the lunar regolith. Thus, we can conclude that the ENAs do not originate from the lunar surface material, but must be reflected solar wind ions.

[40] The best fit of the ENA energy spectra by the Maxwell-Boltzmann distribution indicates that the backscattering mechanism is not a single binary collision, because there the energy would be much higher. Instead, most likely, the backscattered ENAs are generated via multiple collisions off surfaces of regolith grains. Considering the observed average energy spectrum above implies that the ENAs have lost a considerable fraction of their initial energy as solar wind protons. Assuming an energy loss for each collision of typical 10–20% [*Niehus et al.*, 1993], the impinging protons

with an energy of 1 keV (~400 km/s) experience 10–20 of collisions to end up with energy of 100 eV.

[41] Also note that considering the saturation state for hydrogen in the upper crust of the lunar regolith, the total outgoing hydrogen flux must balance the incoming solar wind flux. As the flux of the backscattered ENAs corresponds only 19% of the incoming solar wind protons, different populations of hydrogen atoms outgoing by different mechanisms must exist below the lower limit of the energy range of CENA (~25 eV).

[42] An open question is the proportionality between the ENA temperature and the solar wind velocity, and less so with the solar wind energy. The linear correlation between the ENA temperature and the solar wind velocity (Figure 5) becomes worse if we take the solar wind energy as an explanatory variable. This may indicate that the backscattering processes at the surface might be controlled by the momentum of the impinging particle velocity rather than its energy. If the multiple collisions transfer the solar wind energy to the characteristic energy of the ENAs, kT, this may be proportional to the solar wind energy. However, in our observations the proportionality was found between the ENA temperature and the solar wind bulk velocity. A theoretical model of the backscattering process at the regolith surface is therefore necessary to explain the proportionality.

7. Conclusion

[43] The energy spectra of the ENA flux from the lunar surface are statistically analyzed using the Chandrayaan-1/CENA data set. The energy spectra are fitted best using a Maxwell-Boltzmann distribution. While we also attempt to fit the spectra using a sputtered particle spectrum (Thompson-Sigmund spectrum), the observed flux cannot be reproduced. This indicates that the ENA flux coming from the lunar surface is unlikely sputtered particles from the surface.

[44] We also derived the best fitting parameters for the Maxwell-Boltzmann distribution. We find that the ENA temperature is strongly correlated with the solar wind velocity. The alpha particle flux in the solar wind does not affect the ENA flux from the lunar surface. This is consistent with the above indication that the generation mechanism of ENAs is unlikely of sputtered particle origin. From the reconstructed ENA energy spectra, the backscatter fractions are calculated. The statistical median of the backscatter fraction is 0.19, and the 25% and 75% percentiles are 0.16–0.21. The ratio is fairly constant independent of the upstream solar wind parameters.

[45] The empirical velocity distribution function and the differential flux can be formulated as follows.

$$f(v) = \frac{rF_{SW}}{4\pi}\left(\frac{m}{kT}\right)^2 \exp\left(-\frac{mv^2}{2kT}\right) \quad (17)$$

$$J(E) = \frac{rF_{SW}}{2\pi}\frac{E}{(kT)^2}\exp\left(-\frac{E}{kT}\right) \quad (18)$$

where

$$T[\text{in K}] = V_{SW}[\text{in m/s}] \times 3.17 - 2.31 \times 10^4 \quad (19)$$

and r is the best estimated backscatter fraction of 0.19. As no reliable ionization efficiency of the conversion surface of the CENA sensor is available below 25 eV, the empirical model could be reliably used for the energy range >38 eV.

[46] **Acknowledgment.** We thank the ACE/SWEPAM and ACE/MAG instrument teams and the ACE Science Center for providing the ACE data. We also thank the WIND/SWE instrument team (Principal Investigator K. W. Ogilvie, GSFC/NASA, and A. J. Lazarus, MIT) and the National Space Science Data Center (NSSDC) Space Physics Data Facility (SPDF) for providing the WIND data. The study was supported by the Swedish Research Links Programme funded by the Swedish International Development Cooperation Agency (SIDA).

References

Barabash, S., et al. (2009), Investigation of the solar wind-Moon interaction on board Chandrayaan-1 mission with the SARA experiment, *Curr. Sci.*, *96*(4), 526–532.

Betz, G., and K. Wien (1994), Energy and angular distributions of sputtered particles, *Int. J. Mass Spectrom. Ion Process.*, *140*, 1–110, doi:10.1016/0168-1176(94)04052-4.

Clark, B., B. Hapke, C. Pieters, and D. Britt (2002), Asteroid space weathering and regolith evolution, in *Asteroids III*, edited by W. F. Bottke Jr., 585–599, Univ. of Ariz. Press, Tucson.

Collier, M. R., J. A. Slavin, R. P. Lepping, A. Szabo, and K. Ogilvie (1998), Timing accuracy for the simple planar propagation of magnetic field structures in the solar wind, *Geophys. Res. Lett.*, *25*(14), 2509–2512, doi:10.1029/98GL00735.

Dyal, P., C. W. Parkin, and W. D. Daily (1974), Magnetism and the interior of the Moon, *Rev. Geophys.*, *12*(4), 568–591, doi:10.1029/RG012i004p00568.

Futaana, Y., S. Machida, Y. Saito, A. Matsuoka, and H. Hayakawa (2003), Moon-related nonthermal ions observed by Nozomi: Species, sources, and generation mechanisms, *J. Geophys. Res.*, *108*(A1), 1025, doi:10.1029/2002JA009366.

Futaana, Y., S. Barabash, M. Holmström, and A. Bhardwaj (2006), Low energy neutral atoms imaging of the Moon, *Planet. Space Sci.*, *54*(2), 132–143, doi:10.1016/j.pss.2005.10.010.

Futaana, Y., S. Nakano, M. Wieser, and S. Barabash (2008), Energetic neutral atom occultation: New remote sensing technique to study the lunar exosphere, *J. Geophys. Res.*, *113*, A11204, doi:10.1029/2008JA013356.

Futaana, Y., S. Barabash, M. Holmström, A. Fedorov, H. Nilsson, R. Lundin, E. Dubinin, and M. Fränz (2010), Backscattered solar wind protons by Phobos, *J. Geophys. Res.*, *115*, A10213, doi:10.1029/2010JA015486.

Galli, A., et al. (2008), Tailward flow of energetic neutral atoms observed at Venus, *J. Geophys. Res.*, *113*, E00B15, doi:10.1029/2008JE003096.

Hodges, R. R. (2011), Resolution of the lunar hydrogen enigma, *Geophys. Res. Lett.*, *38*, L06201, doi:10.1029/2011GL046688.

Johnson, R. E., and R. Baragiola (1991), Lunar surface: Sputtering and secondary ion mass spectrometry, *Geophys. Res. Lett.*, *18*(11), 2169–2172, doi:10.1029/91GL02095.

Kazama, K. (2006), Simulation report of the ENA instrument, *IRF Sci. Rep. 289*, Swed. Inst. of Space Phys., Kiruna.

Lin, R. P., D. L. Mitchell, D. W. Curtis, K. A. Anderson, C. W. Carlson, J. McFadden, M. H. Acuña, L. L. Hood, and A. Binder (1998), Lunar surface magnetic fields and their interaction with the solar wind: Results from Lunar Prospector, *Science*, *281*(5382), 1480–1484, doi:10.1126/science.281.5382.1480.

Lopez, R. E., and J. W. Freeman (1986), Solar wind proton temperature-velocity relationship, *J. Geophys. Res.*, *91*(A2), 1701–1705, doi:10.1029/JA091iA02p01701.

Los, J., and J. J. C. Geerlings (1990), Charge exchange in atom-surface collisions, *Phys. Rep.*, *190*(3), 133–190, doi:10.1016/0370-1573(90)90104-A.

Lue, C., Y. Futaana, S. Barabash, M. Wieser, M. Holmström, A. Bhardwaj, M. Dhanya, and P. Wurz (2011), Strong influence of lunar crustal fields on the solar wind flow, *Geophys. Res. Lett.*, *38*, L03202, doi:10.1029/2010GL046215.

McComas, D. J., et al. (2009), Lunar backscatter and neutralization of the solar wind: First observations of neutral atoms from the Moon, *Geophys. Res. Lett.*, *36*, L12104, doi:10.1029/2009GL038794.

Mitchell, D., J. Halekas, R. Lin, S. Frey, L. Hood, M. H. Acuña, and A. Binder (2008), Global mapping of lunar crustal magnetic fields by Lunar Prospector, *Icarus*, *194*(2), 401–409, doi:10.1016/j.icarus.2007.10.027.

Ness, N. F., K. W. Behannon, C. S. Scearce, and S. C. Cantarano (1967), Early results from the magnetic field experiment on Lunar Explorer 35, *J. Geophys. Res.*, *72*(23), 5769–5778, doi:10.1029/JZ072i023p05769.

Niehus, H., W. Heiland, and E. Taglauer (1993), Low-energy ion scattering at surfaces, *Surf. Sci. Rep.*, *17*(4–5), 213–303, doi:10.1016/0167-5729(93)90024-J.

Paularena, K. I., G. N. Zastenker, J. Lazarus, and P. A. Dalin (1998), Solar wind plasma correlations between IMP 8, Interball-1, and WIND, *J. Geophys. Res.*, *103*(A7), 14,601–14,617, doi:10.1029/98JA00660.

Rodríguez, D. F. M., L. Saul, P. Wurz, S. A. Fuselier, H. O. Funsten, D. J. McComas, and E. Möbius (2012), IBEX-Lo observations of energetic neutral hydrogen atoms originating from the lunar surface, *Planet. Space Sci.*, *60*(1), 297–303, doi:10.1016/j.pss.2011.09.009.

Russell, C. T., and B. R. Lichtenstein (1975), On the source of lunar limb compressions, *J. Geophys. Res.*, *80*(34), 4700–4711, doi:10.1029/JA080i034p04700.

Saito, Y., et al. (2008), Solar wind proton reflection at the lunar surface: Low energy ion measurement by MAP-PACE onboard SELENE (KAGUYA), *Geophys. Res. Lett.*, *35*, L24205, doi:10.1029/2008GL036077.

Schaufelberger, A., et al. (2011), Scattering function for energetic neutral hydrogen atoms off the lunar surface, *Geophys. Res. Lett.*, *38*, L22202, doi:10.1029/2011GL049362.

Stern, S. A. (1999), The lunar atmosphere: History, status, current problems, and context, *Rev. Geophys.*, *37*(4), 453–491, doi:10.1029/1999RG900005.

Thompson, M., II (1968), the energy spectrum of ejected atoms during the high energy sputtering of gold, *Philos. Mag.*, *18*, 377–414, doi:10.1080/14786436808227358.

Wieser, M., et al. (2009), Extremely high reflection of solar wind protons as neutral hydrogen atoms from regolith in space, *Planet. Space Sci.*, *57*, 2132–2134, doi:10.1016/j.pss.2009.09.012.

Wieser, M., et al. (2010), First observation of a mini-magnetosphere above a lunar magnetic anomaly using energetic neutral atoms, *Geophys. Res. Lett.*, *37*, L05103, doi:10.1029/2009GL041721.

Wurz, P., and H. Lammer (2003), Monte-Carlo simulation of Mercury's exosphere, *Icarus*, *164*(1), 1–13, doi:10.1016/S0019-1035(03)00123-4.

Wurz, P., U. Rohner, J. A. Whitby, C. Kolb, H. Lammer, P. Dobnikar, and J. A. Martín-Fernández (2007), The lunar exosphere: The sputtering contribution, *Icarus*, *191*(2), 486–496, doi:10.1016/j.icarus.2007.04.034.